



Large-scale numerical simulations of ion beam instabilities in unmagnetized astrophysical plasmas

M. E. Dieckmann, P. Ljung, A. Ynnerman, and K. G. McClements

Citation: *Phys. Plasmas* **7**, 5171 (2000); doi: 10.1063/1.1319640

View online: <http://dx.doi.org/10.1063/1.1319640>

View Table of Contents: <http://pop.aip.org/resource/1/PHPAEN/v7/i12>

Published by the [American Institute of Physics](#).

Related Articles

Energy enhancement of proton acceleration in combinational radiation pressure and bubble by optimizing plasma density

Phys. Plasmas **19**, 083103 (2012)

Quasi-monoenergetic protons accelerated by laser radiation pressure and shocks in thin gaseous targets

Phys. Plasmas **19**, 073116 (2012)

Versatile shaping of a relativistic laser pulse from a nonuniform overdense plasma

Phys. Plasmas **19**, 073114 (2012)

Zonal flows in stellarators in an ambient radial electric field

Phys. Plasmas **19**, 072316 (2012)

Collisional effects on the oblique instability in relativistic beam-plasma interactions

Phys. Plasmas **19**, 072709 (2012)

Additional information on Phys. Plasmas

Journal Homepage: <http://pop.aip.org/>

Journal Information: http://pop.aip.org/about/about_the_journal

Top downloads: http://pop.aip.org/features/most_downloaded

Information for Authors: <http://pop.aip.org/authors>

ADVERTISEMENT

An advertisement for AIP Advances. The top part features the 'AIP Advances' logo in green and yellow, with a series of yellow circles of varying sizes to its right. Below the logo, the text 'Special Topic Section: PHYSICS OF CANCER' is written in white on a dark green background. At the bottom, the text 'Why cancer? Why physics?' is written in yellow, and a blue button with white text says 'View Articles Now'. The background of the advertisement is a green and white abstract pattern of flowing lines.

AIP Advances

Special Topic Section:
PHYSICS OF CANCER

Why cancer? Why physics? [View Articles Now](#)

Large-scale numerical simulations of ion beam instabilities in unmagnetized astrophysical plasmas

M. E. Dieckmann, P. Ljung, and A. Ynnerman

Institute of Technology and Natural Science, Linköping University, Campus Norrköping, 601 74 Norrköping, Sweden

K. G. McClements

EURATOM/UKAEA Fusion Association, Culham Science Centre, Abingdon, Oxfordshire OX14 3DB, United Kingdom

(Received 2 May 2000; accepted 28 August 2000)

Collisionless quasiperpendicular shocks with magnetoacoustic Mach numbers exceeding a certain threshold are known to reflect a fraction of the upstream ion population. These reflected ions drive instabilities which, in a magnetized plasma, can give rise to electron acceleration. In the case of shocks associated with supernova remnants (SNRs), electrons energized in this way may provide a seed population for subsequent acceleration to highly relativistic energies. If the plasma is weakly magnetized, in the sense that the electron cyclotron frequency is much smaller than the electron plasma frequency ω_p , a Buneman instability occurs at ω_p . The nonlinear evolution of this instability is examined using particle-in-cell simulations, with initial parameters which are representative of SNR shocks. For simplicity, the magnetic field is taken to be strictly zero. It is shown that the instability saturates as a result of electrons being trapped by the wave potential. Subsequent evolution of the waves depends on the temperature of the background protons T_i and the size of the simulation box L . If T_i is comparable to the initial electron temperature T_e , and L is equal to one Buneman wavelength λ_0 , the wave partially collapses into low frequency waves and backscattered waves at around ω_p . If, on the other hand, $T_i \gg T_e$ and $L = \lambda_0$, two high frequency waves remain in the plasma. One of these waves, excited at a frequency slightly lower than ω_p , may be a Bernstein–Greene–Kruskal mode. The other wave, excited at a frequency well above ω_p , is driven by the relative streaming of trapped and untrapped electrons. In a simulation with $L = 4\lambda_0$, the Buneman wave collapses on a time scale consistent with the excitation of sideband instabilities. Highly energetic electrons were not observed in any of these simulations, suggesting that the Buneman instability can only produce strong electron acceleration in a magnetized plasma. [S1070-664X(00)02712-9]

I. INTRODUCTION

Beam–plasma streaming instabilities provide a possible energy source for electron acceleration in astrophysical shocks, in particular shocks associated with supernova remnants (SNRs). *In situ* measurements at the bow shock of the earth,¹ hybrid simulations (which treat ions as particles and electrons as a fluid),² and theoretical analyses^{3,4} all indicate that ions are reflected from quasiperpendicular collisionless shocks with sufficiently high Alfvénic Mach numbers (the term “quasiperpendicular” is applicable when the angle between the shock normal and the upstream magnetic field exceeds 45°). The reflected ions gyrate in the upstream field, return to the shock front, and penetrate it, eventually thermalizing in the downstream region. The upstream gyration gives rise to a “foot” region, with spatial dimensions of the order of a reflected ion Larmor radius, in which there are two ion beams: one propagating away from the shock, the other toward it.⁵ The beams constitute a source of free energy in the upstream plasma, and thus instabilities may develop.^{5–9} An understanding of these instabilities, and their saturation mechanisms, is essential for the development of fully self-consistent models of the shock structure and of particle ac-

celeration. In the case of SNRs, there is a need to find a mechanism for accelerating electrons from thermal to mildly relativistic energies (“electron injection”), at which their Larmor radii are comparable to those of the ions: diffusive shock acceleration¹⁰ can then produce highly relativistic electron populations, consistent with observed synchrotron spectra extending from radio to x-ray wavelengths.¹¹

In this paper we study specifically the Buneman instability.¹² Our principal motivation for doing so is that it provides a possible mechanism for electron heating and acceleration at quasiperpendicular SNR shocks.^{7–9} In Ref. 7 a multifluid approach was used to describe electron heating in such scenarios, while in Ref. 8 a hybrid code was employed. Both multifluid and hybrid models treat the electrons as a fluid, and thus cannot be used to simulate the evolution of the electron phase space distribution. They can, however, provide a self-consistent description of the shock structure. In this paper we present the results of one-dimensional particle-in-cell (PIC) simulations. The simulation method makes very heavy demands on computer resources, and it is difficult to model self-consistently an entire shock structure with this method, unless one uses an artificial ion to electron

mass ratio and a relatively small number of particles per cell.¹³ However, by prescribing an initial configuration consisting of one or two ion beams, drifting relative to bulk ions and electrons, we can represent conditions likely to occur at quasiperpendicular high Mach number shocks, thereby obtaining information on acceleration efficiency and the linear and nonlinear processes that may be relevant to electron injection. We employ the electromagnetic and fully relativistic PIC code described in Ref. 14. It solves the Vlasov–Maxwell equations for both electrons and ions, the particle species being represented by computational superparticles in phase space. Superparticles have the same charge to mass ratio as real particles, but the absolute values of charge and mass are larger: This reduces the number of plasma particles in the system, thereby making the kinetic equations computationally tractable.

The nonlinear evolution of the Buneman instability has been studied previously in detail, both analytically^{15,16} and numerically, using PIC simulations.¹⁷ These studies have concentrated on the case of an entire electron population drifting with respect to stationary ions. To model wave excitation and particle acceleration at high Mach number shocks, it is more appropriate to consider a scenario in which instability drive is provided by a component of the ion population which is drifting with respect to stationary electrons and bulk (nonreflected) ions. The term “Buneman instability” is still appropriate in these circumstances. It will be shown that the bulk ions do not merely provide charge neutrality but play an important active role in determining the nonlinear evolution of the plasma. Several authors have studied the nonlinear damping of prescribed, large-amplitude, counterpropagating waves by solving numerically the electrostatic Vlasov–Poisson system of equations.^{18,19} Our approach differs from this in several respects: first, instead of defining the initial parameters of the waves, we prescribe particle distributions which generate the waves from a noise level and continue to drive them throughout the simulation; second, the parameters of our particle distributions are such that waves propagating in only one direction are subject to strong linear instability; finally, we use an electromagnetic PIC model, with three velocity dimensions, rather than a Vlasov–Poisson model with one velocity dimension. In Ref. 18 only the electron Vlasov equation was solved, the ions being treated as a motionless, neutralizing background. Ion dynamics was included in some of the simulations presented in Ref. 19, the conclusion being that ions did not play a significant role in the evolution of the system. We will show, however, that this conclusion applies only in certain parameter regimes.

In our simulations the Buneman instability grows and saturates on a time scale of order $20 \times 2\pi/\omega_p$, where ω_p is the electron plasma frequency: This is comparable to an analytical estimate obtained in Ref. 20 for the quench time of the Buneman instability, based on the assumption of growth from thermal noise levels. In astrophysical plasmas ω_p is generally higher than the electron cyclotron frequency, ω_{ce} . If ω_p/ω_{ce} is sufficiently large, and the instability drive is sufficiently strong, the Buneman wave is amplified significantly in less than one cyclotron period, and the plasma is

then effectively unmagnetized. Even for values of ω_p/ω_{ce} as low as 10, the magnetic field has a negligible effect on the linear growth of the Buneman instability if the ion beam speed is more than a few times the initial electron thermal speed.⁹ Spacecraft observations in the vicinity of the Earth indicate that up to 25% of the ions upstream of a high Mach number quasiperpendicular shock can be reflected.¹ Hybrid code simulations suggest that the reflected ion fraction may be even higher at astrophysical shocks with Mach numbers exceeding those occurring in the heliosphere.²¹ For perpendicular shocks, the maximum beam speed in the upstream plasma frame is twice the shock speed (specular reflection); generally, the maximum beam speed is less than this (non-specular reflection).⁴ Shock speeds associated with young SNRs are typically around 10^7 m s^{-1} .²² In this paper we assume ion beam velocities which are consistent with shock speeds of this order. If $\omega_p \gg \omega_{ce}$, and reflected beam ions have a drift speed in excess of the electron thermal speed, it is not necessary, in the first instance, to include magnetic field effects. Such effects may, however, play a key role in electron acceleration, e.g., via the surfatron mechanism.²³ In a future paper we will present results from large-scale numerical simulations designed to investigate this process.

In Sec. II we list the initial parameters of the simulations, and then present results obtained for the time evolution of electrostatic fields and electron distributions in simulations with two different values of the bulk ion temperature and different simulation box sizes. In Sec. III these results are interpreted in terms of various linear and nonlinear processes. The results are summarized and discussed in Sec. IV.

II. SIMULATIONS

A. Parameters and initial conditions

We present results obtained from three simulations: two with 90 cells, the other with 360 cells. All three simulation boxes are periodic. Each cell is 2.04 m in length: This is approximately equal to the electron Debye length $\lambda_{De} \approx 1.99 \text{ m}$ at the beginning of each simulation. The maximum wavelength which can be represented in the code is the total box size L , which is equal to 183.6 m $\equiv \lambda_0$ in the simulations with 90 cells and 734.4 m $= 4\lambda_0$ in the simulation with 360 cells (it will become apparent that λ_0 is equal to the wavelength of a Buneman-unstable mode). The minimum wave number is thus $k = k_0 = 2\pi/\lambda_0 = 2\pi/183.6 \text{ m}^{-1}$ in the simulations with $L = \lambda_0$, and $k = k_0/4 = 2\pi/734.4 \text{ m}^{-1}$ in the simulation with $L = 4\lambda_0$. The electrons initially have thermal speed $v_e \equiv (T_e/m_e)^{1/2} = 1.25 \times 10^6 \text{ m s}^{-1}$ (T_e denoting electron temperature in energy units and m_e denoting electron mass), zero mean velocity, plasma frequency $\omega_p = 10^5 \times 2\pi \text{ rad s}^{-1}$, and are represented by 30 375 particles per cell (ppc) in the simulations with $L = \lambda_0$, and 8192 ppc in the simulation with $L = 4\lambda_0$. The initial electron temperature is approximately 9 eV: Temperatures of this order are believed to be representative of the heated interstellar medium (ISM) upstream of SNR shocks.²⁴ The electron density is $n_e \approx 1.2 \times 10^8 \text{ m}^{-3}$: this is rather higher than values quoted in Ref. 24 for the ISM in the vicinity of a SNR. However, because our plasma is unmagnetized, there are essentially only three

time scales in our simulations: the plasma period $2\pi/\omega_p$, the period of the wave excited, and the bounce period of electrons trapped by this wave. It will be shown that the last two of these scale as ω_p^{-1} . Thus, a change in n_e changes only the absolute time scale of the simulation. Since time t is normalized in the simulations to $2\pi/\omega_p$, the results are independent of the absolute value of n_e .

In two of the three simulations the bulk protons have thermal speed $v_i = 2.9 \times 10^5 \text{ m s}^{-1}$, corresponding to a temperature $T_i \approx 900 \text{ eV}$; one of these simulations has $L = \lambda_0$, the other has $L = 4\lambda_0$. In the remaining simulation, $v_i = 2.9 \times 10^4 \text{ m s}^{-1}$ ($T_i = T_e \approx 9 \text{ eV}$) and $L = \lambda_0$. In all three cases the bulk protons have zero mean velocity, plasma frequency $\omega_{pi} = 1.9 \times 10^3 \times 2\pi \text{ rad s}^{-1}$, and are represented by 6000 ppc in the simulations with $L = \lambda_0$ and 1568 ppc in the simulation with $L = 4\lambda_0$. In each simulation there are two counterpropagating proton beams, both with mean speed $v_b = 1.875 \times 10^7 \text{ m s}^{-1}$ and Maxwellian distributions, but with unequal temperatures. These drifts are directed along the positive and negative (x) directions of the simulation box. The forward-propagating beam has thermal speed $3 \times 10^5 \text{ m s}^{-1}$, while the backward-propagating beam has thermal speed $3.75 \times 10^6 \text{ m s}^{-1}$. Each beam has plasma frequency $\omega_{pb} = 953 \times 2\pi \text{ rad s}^{-1}$ and is represented by 13 500 ppc in the simulations with $L = \lambda_0$, and 2048 ppc in the simulation with $L = 4\lambda_0$. The number density of each beam relative to the electron density n_e is taken to be $1/6$, so that the total beam density is $n_e/3$: This is comparable to beam concentrations observed in hybrid code simulations²¹ of shocks with Mach numbers characteristic of SNRs.²² The use of a large number of particles per cell is dictated by the need to reduce to a minimum noise fluctuations of electrons in the high velocity tail of the distribution (the total number of particles in the simulations with $L = \lambda_0$ is almost three orders of magnitude greater than that used in the simulation reported in Ref. 17). The initial velocity distributions of electrons and beam ions are shown in Fig. 1.

Since the ion beam speeds are of the same order as the shock speed, our assumed values of v_b are consistent with sonic Mach numbers $M \sim v_b/c_s \sim 60 - 600$ (depending on T_i), where $c_s \sim (T_i/m_p)^{1/2}$ is the sound speed (m_p being the proton mass). Mach numbers of this order are consistent with those of SNR shocks.²² Our assumed plasma beta is formally infinite, since we have finite pressure and zero magnetic field.

In two of the three simulations, the total simulation time in units of $2\pi/\omega_p$ is $t_{\text{max}} = 145$; in the other simulation, $t_{\text{max}} = 80$. Wave amplitude time series are obtained by Fourier transforming the electrostatic field in the simulation box $E(x, t)$ over the discrete space variable x :

$$A(k_l, t) = 2/N \left| \sum_{n=0}^{N-1} E(x_n, t) \exp((-2\pi i)k_l n/N) \right|. \quad (1)$$

Normalizing to $2/N$ rather than $1/N$ gives the amplitude of $\sin(2\pi k_l x)$ rather than that of $\exp(2i\pi k_l x)$. This makes it possible to compare directly the wave amplitude with the threshold electric field amplitude above which significant numbers of electrons are trapped.

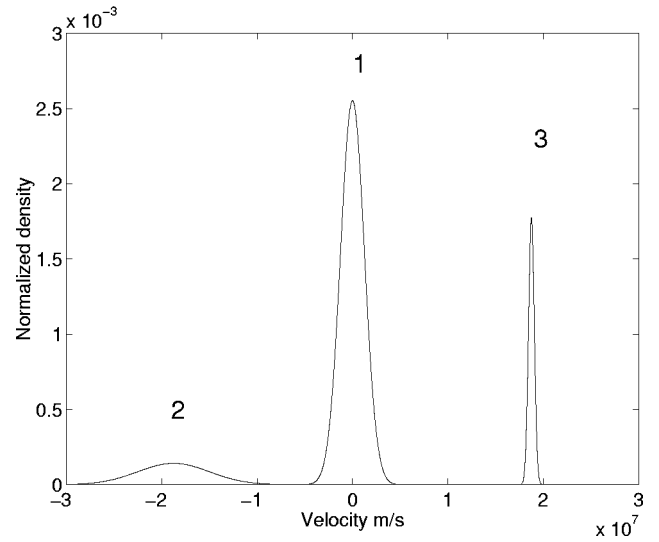


FIG. 1. Initial velocity distributions of (1) electrons, (2) hot beam protons, and (3) cool beam protons used in the simulations. The initial bulk proton distributions would appear as sharp spikes centered on the origin if plotted on the same scale.

Hybrid simulations reported in Ref. 8 indicate that proton beams reflected from high Mach number perpendicular shocks vary on length scales of at least several ion inertial lengths $x_p = c/\omega_{pi}$, where c is the speed of light and ω_{pi} is the total ion plasma frequency. During the time interval of our simulations, the proton beams propagate a total distance $x \approx 57c/\omega_p$. Thus, $x/x_p \approx 57(\omega_{pi}/\omega_p) \sim 1$. The spatial scale of the simulations is thus smaller than the length scale over which the proton beams are likely to vary in a real high Mach number shock, and it is therefore justifiable to prescribe homogeneous beams and periodic boundary conditions in the simulations.

As noted in Ref. 9, the present scenario differs somewhat from that considered originally by Buneman¹² in that ions are drifting with respect to electrons rather than vice versa. This change of frame simply shifts the real frequency of the instability to $|\omega| \approx \omega_p$, while the maximum growth rate,¹²

$$\gamma_{\text{max}} = \left(3 \frac{\sqrt{3}}{16} \omega_{pb}^2 \omega_p \right)^{1/3}, \quad (2)$$

is unaffected. The wave phase speed is approximately equal to the ion drift speed, and so the most unstable wave number is $k = k_{\text{Bun}} \approx \omega_p/v_b \approx 2\pi/187.5 \text{ m}^{-1}$. This is almost exactly equal to the smallest wave number which can be represented in the simulations with $L = \lambda_0$, namely $k_0 = 2\pi/\lambda_0 = 2\pi/183.6 \text{ m}^{-1}$. Setting the box size equal to one wavelength of a large amplitude mode is a common practice in both PIC¹⁷ and Vlasov-Poisson^{18,19} simulations. In Sect. IV we will discuss the reasons for adopting such an approach. Since the Buneman instability has finite bandwidth,¹² one would not expect the slight disparity between k_0 and k_{Bun} in our simulations to cause a significant reduction in the growth rate (similar results were obtained when the simulation box size was set equal to $2\pi/k_{\text{Bun}} \approx 187.5 \text{ m}$). The second lowest wave number permitted by the size of the 90 cell simulation

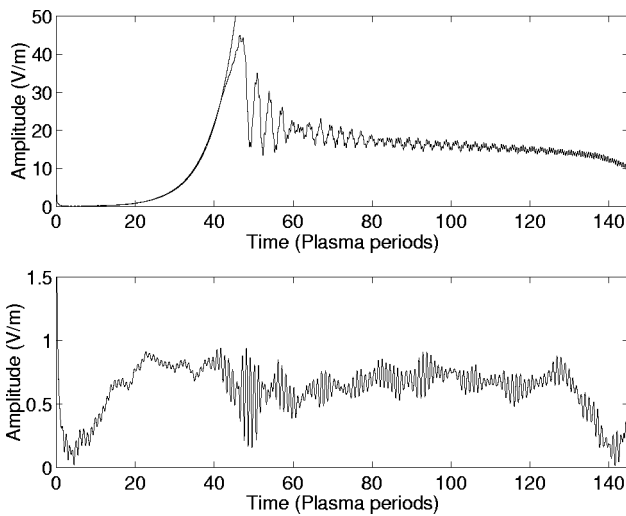


FIG. 2. Wave amplitude at $k=k_0$ vs time for simulation with hot bulk protons and $L=\lambda_0$. The upper and lower plots show, respectively, the wave amplitudes at $\omega>0$ and $\omega<0$.

box, $k=2k_0$, lies well outside the range of unstable Buneman wave numbers. Modes with $k=3k_0/4$ and $k=5k_0/4$ can exist in the simulation with $L=4\lambda_0$: linear stability analysis, using the above-listed distribution function parameters, indicates that the wave at $3k_{\text{Bun}}/4$ is weakly unstable, while the one at $5k_{\text{Bun}}/4$ is damped.

B. Simulation with hot bulk protons and $L=\lambda_0$

Figure 2 shows the time-evolving amplitude of waves with $k=k_0$, $\omega\geq 0$ (upper plot) and $k=k_0$, $\omega\leq 0$ (lower plot). A rectangular window was applied in the discrete (ω, k) space to separate waves with opposite phase velocity v_ϕ . To obtain the time series of waves with $v_\phi>0$, the amplitude spectra of two quadrants with negative v_ϕ were set equal to zero. The data set was then transformed back from (ω, k) space to (x, t) space, and Eq. (1) was used to compute the amplitudes as a function of time. The upper plot in Fig. 2 shows the amplitude of waves with $v_\phi>0$. The mode appearing early in the simulation is driven by the Buneman instability. Between $t=0$ and $t=45$, the amplitude can be well approximated by an exponential fit, the best-fit growth rate being $\gamma/\omega_p=0.025$. The exponential fit, plotted in Fig. 2, begins to diverge from the true amplitude at $t\approx 42$. The amplitude at this time is $E\approx 30 \text{ V m}^{-1}$: we will show later that this is close to the electric field required for particle trapping. After $t\approx 42$ the amplitude oscillates, the magnitude of the oscillations steadily decreasing in time. After $t\approx 130$ the amplitude decreases. The ion beam driving this wave activity loses only a very small fraction of its energy (approximately 0.15%) during the simulation. The waves in the lower plot, with $\omega\leq 0$, are associated with the hot ion beam. In this case there is no exponential growth phase, but there is a buildup in the field amplitude during the first 20 plasma periods. Thereafter, the amplitude remains approximately constant.

Figure 3 shows Fourier power spectra corresponding to the waves shown in Fig. 2. These are normalized to the peak power in the upper plot ($\omega\geq 0$). Three peaks in each spectrum are indicated by vertical lines. Two peaks in the upper

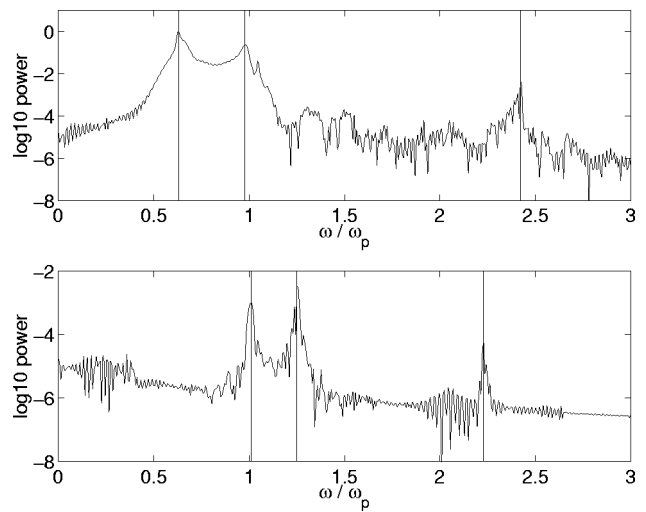


FIG. 3. Power spectra of waves with $\omega>0$ (upper plot) and $\omega<0$ (lower plot) at k_0 for simulation with hot bulk protons and $L=\lambda_0$. Both spectra are normalized to the peak value in the upper plot. Vertical lines indicate peaks at ω_1 , ω_2 , ω_3 (upper plot) and at $\tilde{\omega}_1$, $\tilde{\omega}_2$, $\tilde{\omega}_3$ (lower plot).

plot, at $\omega_1/\omega_p=0.63$ and $\omega_2/\omega_p=0.97$, have similar intensities. The third peak in the upper plot, at $\omega_3/\omega_p=2.42$, is of somewhat lower intensity. Peaks in the lower plot ($\omega<0$) occur at $\tilde{\omega}_1/\omega_p=-1.25$, $\tilde{\omega}_2/\omega_p=-1.01$, and $\tilde{\omega}_3/\omega_p=-2.23$.

The proximity of ω_1 to ω_p enables us to identify it as a Buneman mode.⁹ To facilitate identification of the peaks at ω_1 and ω_3 , we obtain a spectrogram of the waves with $k=k_0$. This was done by Fourier transforming the field data over space, as in Eq. (1) but without taking moduli, thereby generating an amplitude time series. A window Fourier transform was then applied over time at $k=k_0$, using an expression similar to that used in Eq. (1) but with space and wave vector replaced, respectively, by time and frequency. The time domain window for the Fourier transform is rectangular, with width $\Delta t=30\times 2\pi/\omega_p$. A weight of $2/M$, where M is the number of data points inside the window, was assigned to the Fourier transform, again to obtain a sine wave amplitude. In Fig. 4 we show the amplitude spectrum for the interval $(\omega/\omega_p)\in[0.4,1.2]$ (left plot) and $(\omega/\omega_p)\in[2,2.8]$ (right plot). The time variable used in the spectrogram, denoted here by \tilde{t} , corresponds to the center of the Fourier window $[t-\Delta t/2, t+\Delta t/2]$. Amplitude is indicated by a gray scale.

The left-hand plot in Fig. 4 shows immediately that the peaks at ω_1 and ω_2 in Fig. 3 are correlated. Wave growth occurs initially at $\omega\equiv\omega_2\approx\omega_p$, as expected.⁹ At $\tilde{t}\approx 32$ the initial wave bifurcates, with one component remaining at $\omega\approx\omega_p$, the other sweeping down in frequency, eventually reaching a steady value around the frequency ω_1 identified in Fig. 3. By $\tilde{t}\approx 60$, the initial wave at ω_2 has vanished, while the wave at ω_1 remains. The presence of two waves in the time interval $t\in[40,60]$ differing in frequency by $\omega_2-\omega_1\approx\omega_p/3$ gives rise to beat oscillations in the upper plot of Fig. 2. Similar low frequency oscillations occurred in the Vlasov–Poisson simulations presented in Refs. 18 and 19. A

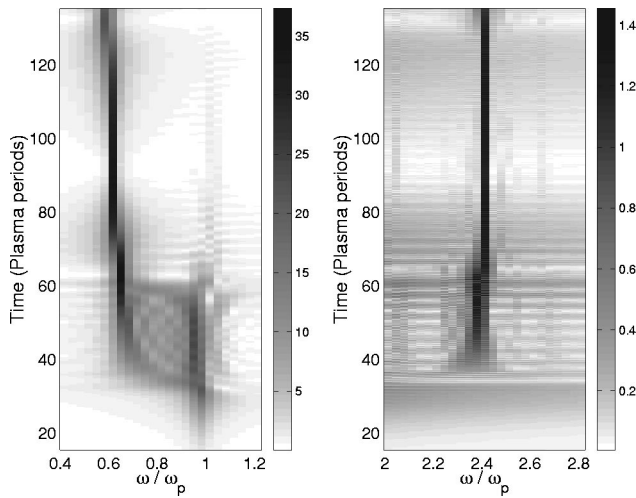


FIG. 4. Spectrogram of waves with $\omega > 0$ close to ω_1 , ω_2 (left-hand plot) and ω_3 (right-hand plot) in simulation with hot bulk protons and $L = \lambda_0$.

corresponding plot for the backward-propagating waves $\bar{\omega}_1$, $\bar{\omega}_2$ shows that these waves follow a similar pattern: the wave energy, initially concentrated at $\bar{\omega}_2$, shifts toward $\bar{\omega}_1$. This shift may have caused the increased oscillation levels after $t \approx 40$ in the lower plot in Fig. 2. The right-hand plot in Fig. 4 shows a wave with $\omega \approx 2.4\omega_p$, which corresponds to the peak at ω_3 in Fig. 3. The amplitude of this wave is much lower than those of the waves at ω_1 and ω_2 . Its first appearance coincides approximately with that of the peak at ω_1 in the left-hand plot. The peak at $\bar{\omega}_3$ is also generated at about the same time.

Figures 5 and 6 show the electron phase space at $t = 41$ and $t = 80$, respectively. At the earlier of these times, the waves at ω_1 , ω_2 , and ω_3 are all present; at the later time, only the waves at ω_1 and ω_3 are still present. Colors from

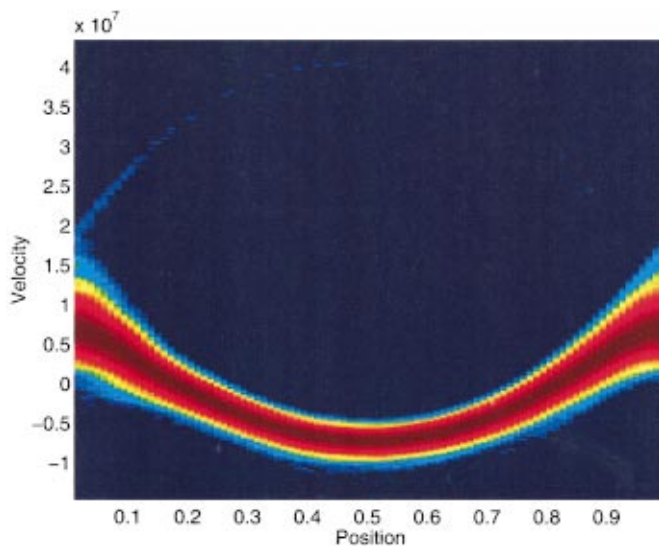


FIG. 5. (Color) Electron phase space at $t = 41$ in simulation with hot bulk protons and $L = \lambda_0$. Colors from dark blue through dark red indicate increasing phase space density. The electron distribution is strongly distorted by a large amplitude wave with $k = k_0$. The light blue arc extending from $x = 0$, $v \approx 2 \times 10^7 \text{ m s}^{-1}$ to higher velocity indicates electron trapping.

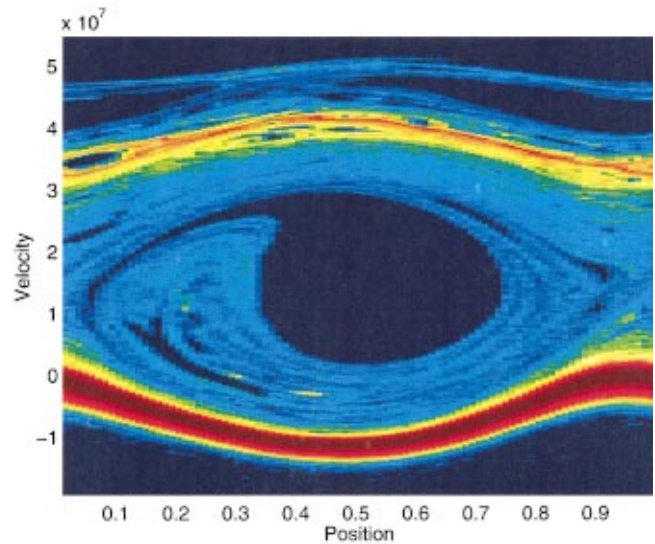


FIG. 6. (Color) Electron phase space at $t = 80$ in simulation with hot bulk protons and $L = \lambda_0$. In addition to the large trapped-particle island which was beginning to appear in the previous figure, there is now a secondary island centered on $v \approx 4.2 \times 10^7 \text{ m s}^{-1}$.

blue through dark red indicate increasing phase space density. Already at $t = 41$ (Fig. 5), the electron distribution is strongly distorted by large amplitude electrostatic waves with $k = k_0$. A small number of electrons form a beam, indicated in Fig. 5 by a light blue arc extending from $x = 0$, $v \approx 2 \times 10^7 \text{ m s}^{-1}$ to higher velocity. This beam has a clearly defined front in coordinate space, moving along the separatrix of a trapped-particle island. By $t = 80$ (Fig. 6) a secondary trapped-particle island has appeared, centered on $v \approx 4.2 \times 10^7 \text{ m s}^{-1}$. Electron beams are apparent above and below this speed. The original trapped-particle island still exists, although significant numbers of electrons are now present close to its center. Electron phase space vortices reminiscent of those appearing in Figs. 5 and 6 have been observed in PIC¹⁷ and Vlasov–Poisson^{18,19} simulations of unmagnetized plasmas with streaming electrons and stationary ions.

C. Simulation with cool bulk protons and $L = \lambda_0$

The time evolution of wave amplitude at $k = k_0$, $\omega \geq 0$ in the simulation with cool bulk protons is shown in the upper plot of Fig. 7. The amplitude increases exponentially up to $t \approx 42$, the growth rate being $\gamma/\omega_p = 0.025$: This is identical to the growth rate observed in the simulation with hot bulk protons. Thus, the linear phase of the instability is essentially independent of bulk proton temperature. Beyond the linear phase, up to $t \approx 60$, the amplitude undergoes oscillations similar to that observed in the simulation with hot bulk protons. Electron phase space plots (not shown here) indicate that particle trapping characteristics are also independent (for this choice of parameters) of the bulk proton temperature. The first differences between the two cases become apparent after $t = 60$: between this time and $t = 74$ (indicated by vertical lines in Fig. 7), the amplitude drops to less than 5 V m^{-1} , and remains at about that level for the remainder

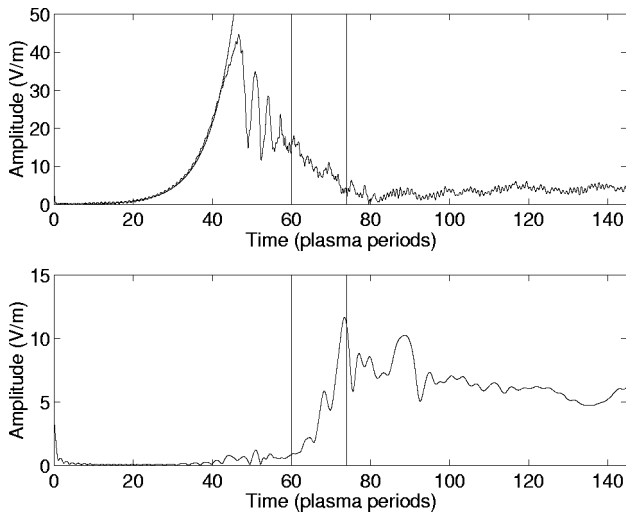


FIG. 7. Wave amplitudes at $k=k_0$, $\omega>0$ (upper plot) and at low ω (lower plot) in simulation with cool bulk protons and $L=\lambda_0$.

of the simulation. The lower plot in Fig. 7 shows wave amplitude $A(t) \equiv (A^2(k_0, t) + A^2(2k_0, t))^{1/2}$ in the range $[-\omega_p/3, \omega_p/3]$. At these frequencies the contribution of $A(2k_0, t)$ to $A(t)$ is significantly greater than that of $A(k_0, t)$, with most wave power concentrated in the two quadrants of the (ω, k) plane with phase speed $v_\phi \equiv \omega/k < 0$. The amplitude of these low frequency waves rises sharply at the same time as the high frequency Buneman wave collapses, between $t=60$ and $t=74$: this is clear evidence of wave energy flowing from high to low frequency modes.

The upper plot in Fig. 8 shows the amplitude of backward-propagating waves with $k=k_0$ and frequencies around $\bar{\omega}_1$, $\bar{\omega}_2$. In the other simulation, the amplitude of backward-propagating waves was approximately constant, and remained below 1 V m^{-1} (see the lower plot in Fig. 2). In Fig. 8, the wave amplitude grows to a much higher level (around 10 V m^{-1}), after the Buneman wave has collapsed and produced the low frequency waves (the period of Bun-

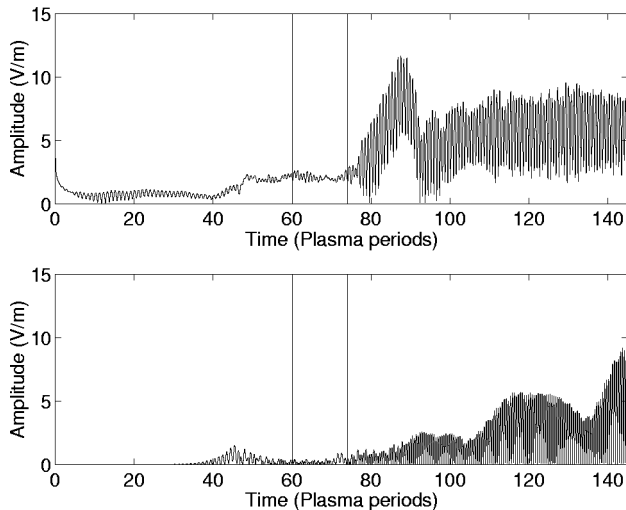


FIG. 8. Mode amplitudes at k_0 , $\omega<0$ (upper plot) and $k=0$ (lower plot) in simulation with cool bulk protons and $L=\lambda_0$.

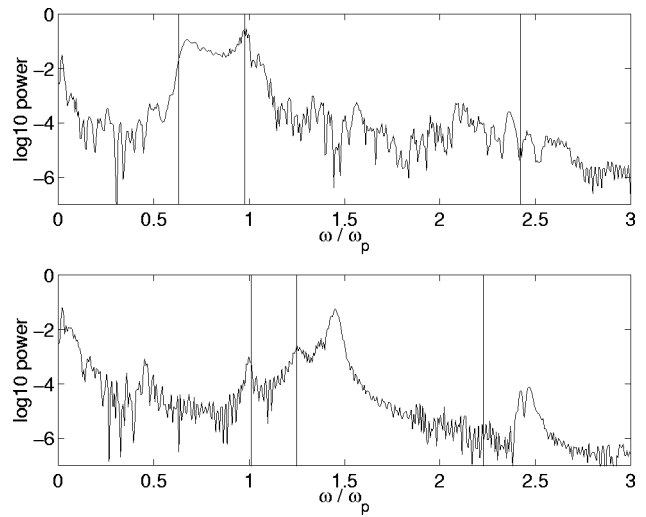


FIG. 9. Power spectra of waves with $k=k_0$, $\omega>0$ (upper plot) and $k=k_0$, $\omega<0$ (lower plot) in simulation with cool bulk protons and $L=\lambda_0$. Both spectra are normalized to the peak value in Fig. 3. Vertical lines indicate the frequencies of the strongest peaks observed in the other simulation (Fig. 3).

eman wave collapse, $t=60-74$, is again indicated by vertical lines). The apparent enhancement in wave amplitude close to $t=0$ in the upper plot is a filter effect. The lower plot in Fig. 8 shows the amplitude of oscillations at $k=0$, $\omega \approx \omega_p$. These also grow after the low frequency waves have been generated, and again reach a peak amplitude of around 10 V m^{-1} , but there is no correlation with the time evolution in the upper plot. It thus appears that the backward-propagating mode with $k=k_0$ and the mode with $k=0$ have different excitation mechanisms.

Figure 9 shows Fourier spectra of waves with $k=k_0$ and $\omega \geq 0$ (upper plot), $\omega \leq 0$ (lower plot). The normalization of wave power is the same as that used in Fig. 3. In the upper plot, vertical lines indicate the frequencies $\bar{\omega}_1$, $\bar{\omega}_2$, and $\bar{\omega}_3$ of the principal maxima in the upper plot of Fig. 3. A strong peak again appears close to $\bar{\omega}_2 \approx \omega_p$, with a slightly less intense one occurring in the vicinity of $\bar{\omega}_1$. In fact, the spectra in the upper plots of Figs. 3 and 9 are fairly similar in the frequency range $0.5\omega_p - 1.3\omega_p$. Outside this range, there are significant differences between the two simulations: The spectrum in Fig. 9 does not contain a peak at $\omega \approx \bar{\omega}_3$, and there is a broadband feature at low frequency which does not appear in Fig. 3. The peak of this broadband feature lies below the ion plasma frequency. The lower plot in Fig. 9 shows the power spectrum for $\omega \leq 0$. Vertical lines indicate the frequencies $\bar{\omega}_1$, $\bar{\omega}_2$, and $\bar{\omega}_3$ of the principal maxima in the lower plot of Fig. 3. In Fig. 9, there are peaks at $\bar{\omega}_1$ and $\bar{\omega}_2$, but the strongest feature occurs at $\omega \approx -1.45\omega_p$. There are also peaks at $\omega \approx -2.4\omega_p$, close to $\bar{\omega}_3$, and at $\omega \approx -0.45$. The low frequency component is slightly broader and stronger at $\omega < 0$ than it is at $\omega > 0$.

We have generated spectrograms of the waves in the upper plot of Fig. 9, using the same procedure as before: The results are shown in Fig. 10. The left-hand plot shows that the Buneman wave at $\omega \approx \bar{\omega}_2 \approx \omega_p$ follows a pattern which is similar to that observed in the simulation with hot bulk pro-

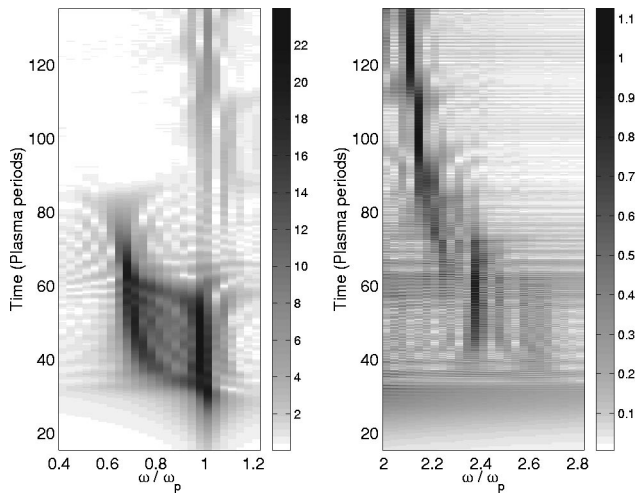


FIG. 10. Spectrogram of waves at $\omega > 0$ close to ω_1 , ω_2 (left-hand plot) and ω_3 (right-hand plot) in simulation with cool bulk protons and $L = \lambda_0$.

tons. After the onset of electron trapping, the Buneman wave decays, and a second wave is generated at $\omega \approx \omega_1$. In contrast to the previous simulation, the wave at ω_1 in Fig. 10 rapidly decays after $\tilde{t} \approx 70$, and has completely disappeared by $\tilde{t} = 80$. The Fourier amplitudes plotted in Fig. 10 are lower than those in Fig. 4, despite similar peak electric fields in the two simulations, because in Fig. 10 the waves have shorter lifetimes (as before, the Fourier transform window has a width of 30 plasma periods). The right-hand plot of Fig. 10 shows the evolution of a wave at $\omega \approx \omega_3$. As in the previous simulation, a wave at this frequency grows at about the same time as the wave at ω_1 . After the latter has collapsed, the wave at ω_3 cascades down in frequency. Because this wave is spread over a broad frequency range, it does not give rise to a strong peak in Fig. 9.

Figure 11 shows spectrograms for the backward-propagating waves. Those with frequencies $|\omega| \leq 1.6\omega_p$ have a wide dynamic range, and for this reason a \log_{10} scale is used in the left-hand plot. The wave at $\omega \approx -\omega_p$, noted pre-

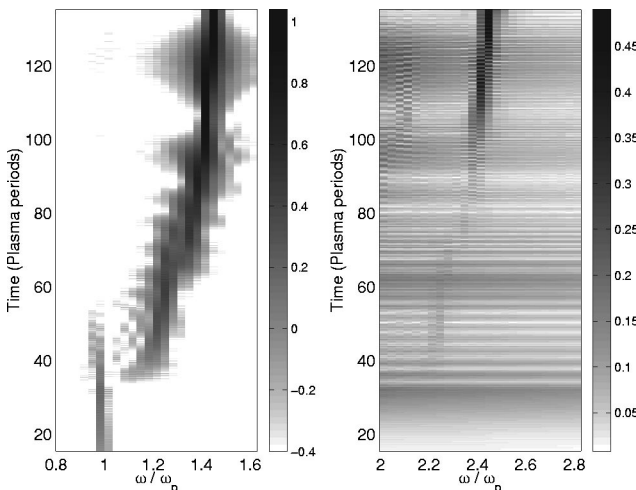


FIG. 11. Spectrogram of waves at $\omega < 0$ close to $\bar{\omega}_1$, $\bar{\omega}_2$ (left-hand plot) and $\bar{\omega}_3$ (right-hand plot) in simulation with cool bulk protons and $L = \lambda_0$. The amplitude in the left-hand plot is displayed on a \log_{10} scale.

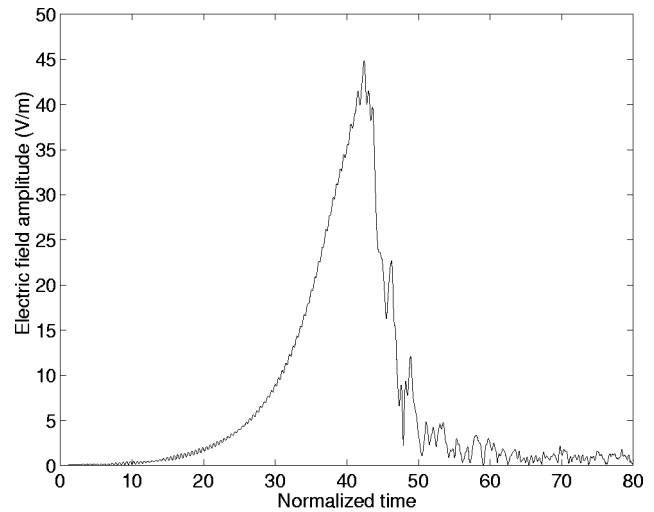


FIG. 12. Wave amplitude at $k = k_0$ vs time for simulation with hot bulk protons and $L = 4\lambda_0$.

viously in the lower plot of Fig. 9, appears early in the simulation, and has approximately constant amplitude up to $\tilde{t} \approx 40$. At this time, there is a shift in frequency to $\omega \approx -1.2\omega_p$. Both amplitude and frequency increase steadily thereafter, the latter converging to $\omega \approx -1.45\omega_p$. Fourier analysis at $|\omega| < 0.8\omega_p$ reveals that the spectral feature at $\omega \approx -0.45\omega_p$ in the lower plot of Fig. 9 first appears at the same time as the low frequency waves associated with Buneman wave collapse. The right-hand plot of Fig. 11 shows that the wave at $\omega \approx -2.4\omega_p$ in the lower plot of Fig. 9 only begins to grow after $\tilde{t} \approx 90$. In contrast, the wave at $\bar{\omega}_3$ in the previous simulation grows at the same time as those at ω_1 and ω_3 .

D. Simulation with hot bulk protons and $L = 4\lambda_0$

Figure 12 shows the time-evolving amplitude of waves with $k = k_0$, $\omega > 0$ in the simulation with hot bulk protons and $L = 4\lambda_0$. The essential difference between this case and that of the simulation with hot bulk protons and $L = \lambda_0$ is that the plasma can now support waves with k equal to any multiple of $k_0/4$: previously, k was restricted to multiples of k_0 . As in the other simulations, there is a phase of exponential growth, with $\gamma/\omega_p \approx 0.025$. However after reaching a peak similar to that observed in the other simulations, the amplitude of the wave with $k = k_0$ rapidly declines from 45 to about 1 V m^{-1} . Similar results were obtained in earlier simulations of magnetized plasmas with box sizes equal to several Buneman mode wavelengths.⁹

III. INTERPRETATION

A. Linear instability

Substituting in Eq. (2) the beam proton concentration used in the simulations (1/6), we obtain $\gamma_{\max} \approx 0.03\omega_p$. The small difference between this figure and the growth rate corresponding to the exponential curves in Figs. 2, 7, and 12 ($0.025\omega_p$) can be largely accounted for by the finite temperatures of the electrons and beam protons: Equation (2) is

applicable only in the cold plasma limit. The exact dispersion relation for an unmagnetized plasma with m Maxwellian particle species is²⁵

$$1 + \sum_{j=1}^m \frac{\omega_{pj}^2 [1 + \zeta_j Z(\zeta_j)]}{k^2 v_j^2} = 0, \quad (3)$$

where ω_{pj} , v_j denote plasma frequencies and thermal speeds, while Z denotes the plasma dispersion function, with arguments $\zeta_j = (\omega - kv_{dj})/\sqrt{2}kv_j$, v_{dj} being the drift speed of species j . Equation (3) can be readily solved numerically for parameters corresponding to the initial conditions of our three simulations. In the case of forward-propagating waves, we obtain a maximum growth rate $\gamma \approx 0.027\omega_p$, at real frequency $\omega \approx 0.994\omega_p$. The corresponding values for backward-propagating waves are $\gamma \approx 0.0012\omega_p$ and $\omega \approx -1.004\omega_p$. This disparity in growth rates is due entirely to the difference in beam temperatures. Although the hot beam excites a Buneman instability, the growth time is of the order of the total simulated time interval ($t = 145$). In fact, as noted previously, there is no evidence from Fig. 2 that such waves undergo a phase of exponential growth. The fact that backward-propagating waves are nevertheless present may be due to statistical fluctuations in particle numbers. As time progresses, these cause a buildup in electrostatic fields: An equilibrium is eventually established between the noise electric fields and the particle density fluctuations, so that the mean amplitude remains approximately constant. Despite the absence of exponentially growing waves with $\omega < 0$, the sharp peak close to $-\omega_p$ in the lower plot of Fig. 3 indicates that the Buneman wave is still a normal mode of the plasma in this case. Moreover, the small difference between ω_2 and $|\bar{\omega}_2|$ is consistent with the difference, noted previously, between the frequencies of the most unstable forward- and backward-propagating waves.

B. Trapped-electron instabilities

The results in Figs. 2, 4, 5, and 12 suggest that the Buneman instability is quenched when the wave amplitude becomes sufficiently large for significant numbers of electrons to be trapped: This was also found to be the case in the PIC simulations reported in Ref. 17. The criterion for a single electron to be trapped is that its velocity component in the propagation direction of the wave differs from the wave phase speed v_ϕ by less than

$$v_{\text{tr}} = \left(2 \frac{eE}{m_e k} \right)^{1/2}, \quad (4)$$

where $-e$ is the electron charge. Trapped electrons which lie close to the center of the wave potential well undergo simple harmonic oscillations with frequency²⁶

$$\omega_b = \left(\frac{ekE}{m} \right)^{1/2}. \quad (5)$$

Large numbers of electrons are trapped if $v_\phi - v_{\text{tr}} \approx v_e$. Care must be exercised in applying this criterion to our simulation results, for several reasons. First, electrons are present in significant numbers with speeds greater than the initial value

of v_e . Second, as Figs. 5 and 6 show, the large amplitude Buneman wave causes the mean velocity of the electron distribution to oscillate. Finally, when more than one trapped-particle island exists, as in Fig. 6, neighboring islands interact in such a way that the half-widths are modified.²⁷ These caveats notwithstanding, we can obtain from Eq. (4) the electric field amplitude at which the Buneman wave traps a significant fraction of the electron population:

$$E_{\text{trap}} = \frac{m_e k_0}{2e} (v_\phi - v_e)^2. \quad (6)$$

The phase velocity of the Buneman wave v_ϕ is approximately equal to v_b , and so $v_\phi - v_e \approx 1.75 \times 10^7 \text{ m s}^{-1}$. Using $k_0 = 2\pi/183.6$, we obtain $E_{\text{trap}} \approx 30 \text{ V m}^{-1}$. The exponential curves in Figs. 2 and 7 begin to depart from the actual wave amplitudes when the latter reach precisely this value. Our conjecture that saturation of the initial instability can be attributed to electron trapping is thus confirmed. Given that E saturates at a value close to E_{trap} , the phase speed v_ϕ is much greater than the electron thermal speed v_e , and $v_\phi \approx \omega_p/k_0$, it follows from Eqs. (5) and (6) that ω_b at saturation scales with ω_p .

Secondary instabilities are driven by the streaming between trapped and untrapped particles. In Ref. 26 it is shown that if all the trapped particles remain close to the center of the wave potential, instability occurs at wave numbers above and below that of the large amplitude wave, the maximum drive occurring at frequencies close to $\omega \pm \omega_b$, where ω is the large amplitude wave frequency. However, the analysis in Ref. 26 cannot be used to interpret the results obtained in simulations with $L = \lambda_0$, since in those cases k is restricted to multiples of $k_0 \approx k_{\text{Bun}}$. Moreover, it is clear from Figs. 5 and 6 that the trapped electrons lie close to the separatrix of the trapped-particle island, rather than the center: This arises simply from the fact that we prescribed an initial electron distribution which was Maxwellian, and hence monotonic decreasing in speed. An electron lying precisely at the separatrix has zero bounce frequency. An advantage of using a box size equal to one wavelength is that it allows us to investigate numerically the effect of an isolated trapped-electron instability when the particles driving the mode cannot be treated as simple harmonic oscillators. In Ref. 28 it is noted that an electron distribution with two components, one drifting with respect to the other with speed v_d , can drive unstable either an electron plasma wave, with $\omega^2 \approx \omega_p^2 + 3k^2 v_e^2$, or a beam mode, with $\omega \approx kv_d$. Which of these two instabilities has the lower threshold depends on the density and temperature of the drifting electrons, and the drift speed. The mode at $\omega \approx 2.4\omega_p$ in Fig. 4 has $k = k_0$ and hence phase speed $v_\phi \approx 2.4\omega_p/k_0 \approx 4.4 \times 10^7 \text{ m s}^{-1}$, which is approximately equal to both the maximum speed of electrons at the separatrix of the trapped-particle island in Fig. 5, and the center of the secondary trapped-particle island in Fig. 6. This is clear evidence that the wave at $2.4\omega_p$ is a trapped-electron beam mode.

It appears likely that the modes at $0.6\text{--}0.7\omega_p$ in Figs. 4 and 10 are also associated with trapped electrons: their excitation is correlated with both the onset of trapping (cf. Fig.

5) and the trapped-electron instability at higher frequency. They may represent Bernstein–Greene–Kruskal (BGK) modes: exact solutions of the unmagnetized Vlasov and Poisson equations in one dimension, propagating at a unique speed v_0 in the plasma frame.²⁹ In this frame the electrostatic potential ϕ is time independent and satisfies a nonlinear Poisson equation of the form³⁰

$$\frac{d^2\phi}{dx^2} = -\frac{2}{\epsilon_0} \sum_{j=1}^m q_j \int_{q_j\phi(x)}^{\infty} \frac{f_j(\mathcal{E})d\mathcal{E}}{\sqrt{2m_j[\mathcal{E}-q_j\phi(x)]}}, \quad (7)$$

where ϵ_0 is free space permittivity and, as in Eq. (3), the summation is over particle species, $f_j(\mathcal{E})$ denoting the distribution in $\mathcal{E} \equiv m_j v_{xj}^2/2 + q_j\phi(x)$ of species j with mass m_j and charge q_j (v_{xj} is the x velocity component in the frame in which ϕ is stationary). Integrating by parts the right-hand side of Eq. (7), and differentiating both sides with respect to x , one finds that $\phi(x)$ is aperiodic if all the distributions are monotonic decreasing in \mathcal{E} .³⁰ If, on the other hand, at least one species has $\partial f_j/\partial \mathcal{E} > 0$ for a range of values of \mathcal{E} , there is a possibility of obtaining spatially periodic solutions of Eq. (7) which, in the plasma frame, have wave-like characteristics. Because the simulation boxes with $L = \lambda_0$ constrain k to be equal to k_0 or multiples thereof, the frequencies $\omega = kv_0$ of such waves would be integer multiples of k_0v_0 . The lowest such multiple would match that of the modes at 0.6–0.7 ω_p in Figs. 4 and 10 if the speed v_0 of the frame in which ϕ is stationary were of the order of, but somewhat lower than, the beam speed v_b . In the case of the simulation with hot bulk protons and $L = \lambda_0$ (Fig. 4), the mode in question is in equilibrium with the trapped and untrapped particle populations, and thus exhibits the essential characteristic of a BGK mode. Evidence for steady-state nonlinear waves of this type was also found in Vlasov–Poisson simulations reported in Ref. 19. In these simulations, two counterpropagating waves were initially present in the plasma: the asymptotic state of the system was characterized by what appear to have been two counterpropagating BGK waves. In our case, the ion beams initially excite only one large amplitude wave, and so one would expect only a single BGK-like mode to appear in the nonlinear phase.

In the simulation with $L = 4\lambda_0$, it appears that waves with $k = k_0$ decline rapidly in amplitude because of secondary instabilities at $k = nk_0/4$ ($n = 1, 2, 3, \dots$). Our results can be compared with Vlasov–Poisson simulations carried out by Brunetti and co-workers¹⁹ with a box size equal to four wavelengths of an imposed large amplitude mode. It was found in this case that upper and lower sideband waves associated with trapped electrons²⁶ were excited at $k = 3k_0/4$ and $5k_0/4$. The amplitude of the lower sideband mode, in particular, rose to a level exceeding that of the original waves at $k = k_0$. At later times, it was found that the electric field power spectrum contained significant contributions from other sidebands, and the amplitude at $k = k_0$ declined further. The growth rate of the sideband instability is essentially determined by two parameters:³¹ ω_b/ω_p and the fraction of trapped electrons, n_{tr}/n_e . The values of these parameters in the PIC simulation discussed here and the Vlasov–Poisson simulation of Ref. 19 are somewhat different, and so

the results are not directly comparable. The wave collapse shown in Fig. 12 of this paper and in Fig. 5 of Ref. 19 includes the waves identified as BGK modes, since these too have $k = k_0$. Perturbative analyses of the sideband instability^{26,31} are not strictly applicable to the results shown in Fig. 12: as noted previously, the majority of trapped electrons in the simulations lie close to the island separatrix, and in any case ω_b is not small compared to ω . It is instructive nevertheless to compare the rate of collapse in Fig. 12 with analytical estimates of the sideband instability maximum growth rate obtained in Ref. 31:

$$\frac{\gamma}{\omega_p} = \epsilon^{2/3} \frac{\sqrt{3} \omega_b}{2^{4/3} \omega_p}, \quad \epsilon \ll 1, \quad (8)$$

$$\frac{\gamma}{\omega_p} = \frac{\sqrt{3}}{2^{4/3}} \left(\frac{n_{tr}}{n_e} \right)^{1/3}, \quad \epsilon \gg 1,$$

where $\epsilon = (n_{tr}/n_e)(\omega_p^3/\omega_b^3)$. For a Maxwellian electron distribution the trapped fraction is given by

$$\frac{n_{tr}}{n_e} = \frac{1}{(2\pi)^{1/2}} \int_{v_{\phi}-v_{tr}}^{v_{\phi}+v_{tr}} e^{-v^2/v_e^2} dv, \quad (9)$$

where the trapping speed v_{tr} is given in terms of the wave electric field amplitude by Eq. (4). It is evident from Eqs. (4) and (9) that the trapped electron fraction is exponentially sensitive to E , which is rapidly evolving in time. Estimates of the instability growth rate based on Eq. (8) are in any case rather uncertain, because of the approximations used to derive it. From Eq. (9) we can, however, infer that the collapse time scale and absolute electric field amplitudes in Fig. 12 are broadly consistent with the growth rate estimate given by Eq. (8). We conclude that the most likely cause of the difference between the hot bulk proton simulations with $L = \lambda_0$ and $L = 4\lambda_0$ is that the waves at $k = k_0$ in the latter were strongly modified by sideband instabilities.

C. Ponderomotive force and low frequency waves

When a wave electric field amplitude exceeds a certain threshold E_c , the resulting ponderomotive force significantly modifies the ion density. For a plasma with Maxwellian bulk ions, the appropriate expression for E_c is³²

$$E_c = \sqrt{4 \frac{m_e}{e^2} \omega^2 T_i}. \quad (10)$$

This threshold is derived by assuming that the bulk ions satisfy a Boltzmann relation, in which the potential has a gradient whose magnitude equals the ponderomotive force divided by e . In our simulations $\omega \approx \omega_p = 10^5 \times 2\pi \text{ rad s}^{-1}$ and T_i was either 900 or 9 eV. In the former case $E_c \approx 90 \text{ V m}^{-1}$, well above the trapping electric field $E_{trap} \approx 30 \text{ V m}^{-1}$ at which the Buneman instability saturates (see Fig. 2). Thus, in the simulation with hot bulk protons one would not expect the ponderomotive force to have any significant effect. For the simulation with cool bulk protons, on the other hand, Eq. (10) gives $E_c \approx 9 \text{ V m}^{-1}$, well below E_{trap} . In this simulation, low frequency wave activity begins to occur at about the time that the Buneman wave amplitude

reaches E_c (Fig. 7): the low frequency waves rise sharply in magnitude when the Buneman wave has fallen from its peak intensity, but still exceeds E_c . As noted in Sec. II, strong excitation of the low frequency mode precipitates a rapid further decline at high frequency. The ponderomotive force is strong enough to create cavities in the proton density, which cause the high frequency waves to collapse. This collapse is apparent in Fig. 7, where the amplitude drops from about 20 V m^{-1} to less than 5 V m^{-1} in the time interval $t = 60\text{--}74$, and also in Fig. 10, where one can see that the high amplitude wave at $\omega \approx 0.6\omega_p$ disappears completely (note that the intensity scale on the right-hand plot of Fig. 10 differs by a factor of 20 from that of the left-hand plot, and therefore the mode cascading down from $\omega \approx 2.4\omega_p$ has a much lower amplitude than the mode at $0.6\omega_p$). We note finally that the Boltzmann relation used to derive Eq. (10) is applicable here, since the low frequency parts of the wave spectra in Fig. 9 include frequencies which are below ω_{pi} , and therefore the inertial term in the bulk ion fluid equation of motion can be neglected.

As noted previously, ion dynamics was not included in the Vlasov–Poisson simulations described in Ref. 18. Brunetti and co-workers,¹⁹ also using a Vlasov–Poisson model, found that ion motion had a negligible effect on the nonlinear evolution of large amplitude waves with $\omega \sim \omega_p$. However, this was due to the fact that they assumed plasma temperatures which were sufficiently high ($\sim 5 \text{ keV}$) that E was always less than E_c . Setting $\omega = \omega_p$ and $T_i = T_e = 5 \text{ keV}$ in Eq. (10), it is straightforward to verify that even the highest electric field amplitude considered in Ref. 19, $E = 0.0375m_e c \omega_p / e$, was about a factor of 5 lower than the threshold for ion density modulations to occur.

D. Parametric instability

The simulation results contain evidence that parametric instabilities also played a role in driving the low frequency waves. The modes shown in Fig. 8 have frequencies of magnitude close to ω_p and wave numbers $k = k_0$ (upper plot) and $k = 0$ (lower plot). We denote the frequency and wave number of an arbitrary low frequency wave by ω_s , k_s , and the corresponding parameters of the modes in Fig. 8 by ω_{L1-} , $k_{L1-} = k_0$ (upper plot) and ω_{L2-} , $k_{L2-} = 0$ (lower plot). As before, we denote the frequency and wave number of the initial Buneman wave by ω_2 , $k_2 = k_0$. Bearing in mind that the wave in the upper plot of Fig. 8 is backward propagating, so that ω_{L1-} is numerically negative (if all wave numbers are defined to be numerically positive), we identify two possible three-wave interactions in which momentum and energy are conserved:

$$\omega_2 + \omega_{L1-} = \omega_s, \quad k_2 + k_{L1-} = k_s, \quad (11)$$

$$\omega_2 - \omega_{L2-} = \omega_s, \quad k_2 - k_{L2-} = k_s. \quad (12)$$

Equation (11) implies $k_s = 2k_0$, while Eq. (12) gives $k_s = k_0$. It is significant that low frequency waves were detected at both values of k in the simulation with cool bulk protons, with amplitudes far exceeding noise levels. Since the three-wave interactions described by Eqs. (11) and (12) are independent, one would expect the amplitudes of the

backscattered high frequency modes $L1-$ and $L2-$ to be also independent. This is consistent with the time evolution of the two modes shown in Fig. 8.

IV. CONCLUSIONS AND DISCUSSION

We have used a PIC code to study the linear and nonlinear evolution of the Buneman instability excited by an ion beam, using plasma parameters which are representative of supernova remnant (SNR) shocks. The Buneman wave saturates primarily as a result of electron trapping. The initial wave, excited at the electron plasma frequency ω_p , is observed to collapse when its amplitude is high enough to trap a significant fraction of the electron population. When wavelengths longer than that of the Buneman wave are excluded from the simulation (by choosing a simulation box size equal to one wavelength), two high frequency waves emerge from the collapse: one with amplitude comparable to that of the Buneman wave and frequency slightly lower than ω_p , the other with lower amplitude and frequency well above ω_p . Both of these modes are amplified to high levels within a few electron plasma periods. The lower frequency wave may be a BGK mode; the higher frequency wave appears to be driven by the streaming between trapped and untrapped electrons, and can be regarded as a beam mode, the beam in this case consisting of electrons lying close to the separatrix of trapped-particle islands. These modes were excited in simulations with both hot ($T_i \gg T_e$) and cool ($T_i \approx T_e$) bulk ions. However, subsequent evolution of the waves was strongly dependent on the bulk ion temperature. When $T_i \gg T_e$ was specified as the initial condition, both high frequency modes remained in the plasma until the end of the simulation. In contrast, when T_i was set approximately equal to T_e , the high amplitude mode collapsed, and the other mode cascaded down in frequency. At the same time waves of much lower frequency ($\omega \sim \omega_{pi}$), excited apparently by a modulational instability, appeared in the plasma. In a simulation with $T_i \gg T_e$ and a box size equal to four Buneman wavelengths, the original wave was observed to collapse on a time scale broadly consistent with the excitation of sideband instabilities and the cascading of wave energy to modes with $k = nk_0/4$ ($n = 1, 2, 3, \dots$), where k_0 is the wave number of the Buneman wave.

In the simulations with short box lengths we excluded waves driven by trapped particle instabilities at $k < k_0$ and $k_0 < k < 2k_0$.^{26,31} The advantage of such an approach is that one can obtain a clearer physical picture of the complex nonlinear interactions between particles and waves by studying the effects of one or two trapped particle modes, which can exist in the plasma for relatively long periods (it should be noted, however, that even in the simulations with short box lengths there are certain phenomena, such as the appearance of a wave at $\omega = \bar{\omega}_3$, whose origin remains unclear). Most of the analytical work which has been carried out on problems of this type (e.g., Ref. 15) also considers the effect of single wave modes, and does not take into account the sideband instabilities which occur when k is unrestricted. Thus, simulations with $L = \lambda_0$ provide a useful link between analytical theory and real plasmas: this type of approach has been used

by a number of authors.^{17–19} In a real plasma, one would expect quasisteady trapped electron modes such as those shown in Fig. 4 to have finite lifetimes, determined principally by the amplitude of the initial large amplitude wave: in Ref. 19 it was concluded that BGK modes can still exist when the simulation box size is greater than one wavelength, for a period of time which decreases with the initial wave amplitude. A conclusion of the present paper is that when the initial wave is generated self-consistently by ion beams of the type known to exist in the vicinity of high Mach number collisionless shocks, the amplitude may be so high that the resulting sideband instabilities prevent BGK-like modes from appearing. It should be stressed, however, that the wave amplitude is strongly dependent on the ion beam parameters, such as the ratio of beam speed to electron thermal speed.⁹ It is thus possible that BGK-like modes of the type discussed here and in Ref. 19 could exist at astrophysical shocks.

One of our motives in carrying out these simulations was to investigate processes which could play a role in electron acceleration. The low frequency waves observed in the simulation with cool bulk protons modified only the low velocity component of the electron distribution, and may in fact have inhibited electron acceleration by causing the high frequency modes at $\omega \sim \omega_p$ to collapse. The simulation with $L=4\lambda_0$ shows that the Buneman wave can also collapse because of sideband instabilities. The results in Ref. 9 indicate that wave collapse does not necessarily prevent high energy electrons from being produced. It does appear, however, that the presence of a magnetic field is a prerequisite for strong acceleration. We do not observe electrons with the mildly relativistic energies required for injection at SNR shocks in any of the simulations discussed here, despite the use of a very large number of particles per cell. Electrons close to the separatrices of the trapped-particle islands resulting from the Buneman instability have speeds of up to $4.4 \times 10^7 \text{ m s}^{-1}$ (Fig. 5), more than twice the proton beam speed v_b . In the case of the simulation with hot bulk protons and $L=\lambda_0$, electrons at the separatrix of the secondary trapped particle island have speeds of nearly $3v_b$. The maximum electron speed v_{max} is limited by v_b and the trapping speed v_{tr} : The latter is also of the order of v_b [cf. Eqs. (4) and (6)]. We infer that v_{max} has a roughly linear dependence on v_b , and so v_{max} would only be of order c if the proton beam and hence the shock were themselves relativistic. However, this limitation applies only to the case of strictly unmagnetized plasmas. In Ref. 9 it was found that strong electron acceleration could be attributed to stochasticity in phase space resulting from the combined effect of a large amplitude electrostatic wave and a magnetic field. In the surfatron process,²³ an electron trapped by an electrostatic wave propagating at phase velocity v_ϕ is accelerated by an electric field $\gamma_\phi \mathbf{v}_\phi \times \mathbf{B}$, where \mathbf{B} is the magnetic field and $\gamma_\phi = (1 - v_\phi^2/c^2)^{-1/2}$. We are in the process of carrying out simulations with initial conditions similar to those invoked here, but with the added feature of a weak magnetic

field. This addition should make it possible to model self-consistently the surfatron process and other magnetic field effects. We will report on these simulations in a later paper.

ACKNOWLEDGMENTS

We would like to thank the National Supercomputer Centre (NSC) of Sweden for providing the computer resources used to carry out this work. The work was supported by the Commission of the European Communities (under TMR Network Contract ERB-CHRXCT980168), the University of Linköping, the United Kingdom Department of Trade and Industry, and EURATOM. Helpful conversations with Bob Bingham (Rutherford Appleton Laboratory) and Jes Christiansen (EURATOM/UKAEA Fusion Association) are gratefully acknowledged.

- ¹N. Scopke, G. Paschmann, S. J. Bame, J. T. Gosling, and C. T. Russell, *J. Geophys. Res.* **88**, 6121 (1983).
- ²M. M. Leroy, D. Winske, C. C. Goodrich, C. S. Wu, and K. Papadopoulos, *J. Geophys. Res.* **87**, 5081 (1982).
- ³L. C. Woods, *J. Plasma Phys.* **3**, 435 (1969).
- ⁴M. Gedalin, *J. Geophys. Res.* **101**, 4871 (1996).
- ⁵K. G. McClements, R. O. Dendy, R. Bingham, J. G. Kirk, and L. O'C. Drury, *Mon. Not. R. Astron. Soc.* **291**, 241 (1997).
- ⁶A. A. Galeev, *Sov. Phys. JETP* **59**, 965 (1984).
- ⁷K. Papadopoulos, *Astrophys. Space Sci.* **144**, 535 (1988).
- ⁸P. J. Cargill and K. Papadopoulos, *Astrophys. J.* **329**, L29 (1988).
- ⁹M. E. Dieckmann, K. G. McClements, S. C. Chapman, R. O. Dendy, and L. O'C. Drury, *Astron. Astrophys.* **356**, 377 (2000).
- ¹⁰A. R. Bell, *Mon. Not. R. Astron. Soc.* **182**, 147 (1997).
- ¹¹R. Willingale, R. G. West, J. P. Pye, and G. C. Stewart, *Mon. Not. R. Astron. Soc.* **278**, 479 (1996).
- ¹²O. Buneman, *Phys. Rev. Lett.* **1**, 8 (1958).
- ¹³N. Shimada and M. Hoshino, "Strong electron acceleration at high Mach number shock waves: Simulation study of electron dynamics," to appear in *Astrophys. J. Lett.*
- ¹⁴P. E. Devine and S. C. Chapman, *J. Geophys. Res.* **100**, 17189 (1995).
- ¹⁵J. A. Ionsion, *Phys. Lett.* **60A**, 27 (1977).
- ¹⁶A. A. Galeev, R. Z. Sagdeev, V. D. Shapiro, and V. I. Shevchenko, *Sov. Phys. JETP* **54**, 306 (1981).
- ¹⁷O. Ishihara, A. Hirose, and A. B. Langdon, *Phys. Fluids* **24**, 452 (1981).
- ¹⁸G. Manfredi, *Phys. Rev. Lett.* **79**, 2815 (1997).
- ¹⁹M. Brunetti, F. Califano, and F. Pegoraro, *Phys. Rev. E* **62**, 4109 (2000).
- ²⁰R. A. Treumann and W. Baumjohann, *Advanced Space Plasma Physics* (Imperial College Press, London, 1997), Chap. 2.3.
- ²¹K. B. Quest, *J. Geophys. Res.* **91**, 8805 (1986).
- ²²D. C. Ellison and S. P. Reynolds, *Astrophys. J.* **382**, 242 (1991).
- ²³T. Katsouleas and J. M. Dawson, *IEEE Trans. Nucl. Sci.* **NS-30**, 3241 (1983).
- ²⁴C. F. McKee and J. P. Ostriker, *Astrophys. J.* **218**, 148 (1977).
- ²⁵F. F. Chen, *Introduction to Plasma Physics and Controlled Fusion* (Plenum, New York, 1984), p. 269.
- ²⁶W. L. Kruer, J. M. Dawson, and R. N. Sudan, *Phys. Rev. Lett.* **23**, 838 (1969).
- ²⁷D. F. Escande, *Phys. Scr.*, T **2/1**, 126 (1982).
- ²⁸P. McQuillan and K. G. McClements, *J. Plasma Phys.* **40**, 493 (1988).
- ²⁹I. B. Bernstein, J. M. Greene, and M. D. Kruskal, *Phys. Rev.* **108**, 546 (1957).
- ³⁰N. A. Krall and A. W. Trivelpiece, *Principles of Plasma Physics* (San Francisco Press, San Francisco, 1986), p. 437.
- ³¹M. V. Goldman and H. L. Berk, *Phys. Fluids* **14**, 801 (1971).
- ³²R. A. Treumann and W. Baumjohann, *Advanced Space Plasma Physics* (Imperial College Press, London, 1997), Chap. 11.1.